Supplement for "Process Modeling of Aerosol-cloud Interaction in Summertime Precipitating Shallow Cumulus over the western North Atlantic"

Xiang-Yu Li[1], Hailong Wang[1], Matthew W. Christensen[1], Jingyi Chen[1], Shuaiqi Tang[1], Simon Kirschler[2], Ewan Crosbie[3,4], Luke D. Ziemba[3], David Painemal[3,4], Andrea F. Corral[5], Kayla Ann McCauley[6], Sanja Dmitrovic[7], Armin Sorooshian[5,6], Marta Fenn[3], Joseph S. Schlosser[5], Snorre Stamnes[3], Johnathan W. Hair[3], Brian Cairns[8], Richard Moore[3], Richard Anthony Ferrare[3], Michael A. Shook[3], Yonghoon Choi[3,4] Glenn S. Diskin[3], Joshua DiGangi[3], John B. Nowak[3], Claire Robinson[3,4], Taylor J. Shingler[3], Kenneth Lee Thornhill[3], Christiane Voigt[2]

[1]Pacific Northwest National Laboratory, Richland, WA, United States

[2]Institut für Physik der Atmosphäre, Deutsches Zentrum für Luft- und Raumfahrt (DLR), Oberpfaffenhofen, Germany, and Institute for Physics of the Atmosphere, Johannes Gutenberg-University Mainz, Germany

[3]NASA Langley Research Center, Hampton, VA, United States

[4]Analytical Mechanics Associates, Hampton, VA, United States

[5]University of Arizona, Department of Chemical and Environmental Engineering, Tucson, AZ, United States

[6]University of Arizona, Department of Hydrology and Atmospheric Sciences, Tucson, AZ, United States

[7]University of Arizona, James C. Wyant College of Optical Sciences, Tucson, AZ, United States

[8]NASA Goddard Institute for Space Studies, New York, NY, United States

Corresponding author: Xiang-Yu Li, `xiangyu.li@pnnl.gov`

Corresponding author: Hailong Wang, `hailong.wang@pnnl.gov`

Table S1: Fitted parameters of the aerosol size distribution below cloud base (BCB) for the 02 and 07 June 2021 cases shown in Figure S4. The percentage error (PE) is defined as $\mathrm{PE} = (\bar{N}_{\mathrm{fit}} - \bar{N}_{\mathrm{a}})/\bar{N}_{\mathrm{a}} \times 100\%$.

Case	Time, UTC	N (cm^{-3})			μ (nm)			σ			$\bar{N}_{\mathrm{a}}$ (cm^{-3})	$\bar{N}_{\mathrm{fit}}$ (cm^{-3})	PE
		N_1	N_2	N_3	μ_1	μ_2	μ_3	σ_1	σ_2	σ_3			
0602	19:00:12-19:08:00	498	204	3.04	23.7	98.5	415.1	1.62	1.38	1.23	707	728	2.9%
0607	19:13:25-19:21:49	2134	136	5.14	28.6	117.1	341.2	1.63	1.25	1.63	2073	2197	6.0%

Table S2: Time-averaged mass concentration $\overline{m}_i$ from the AMS measurement sampled during BCB flight legs for the 02 and 07 June 2021 cases. NaCl is not efficiently sampled by AMS because it is refractory (i.e., not volatile at 600 Pa), and therefore the Cl mass is likely not representative of NaCl mass. The AMS measurement is only for aerosol particles in the size (diameter) range 60-600 nm approximately.

Case	Organic	Sulfate (SO_4^{2-})	Nitrate (NO_3^-)	Ammonium (NH_4^+)
0602	11.0%	74.8%	1.5%	11.2%
0607	46.1%	38.8%	2.6%	11.6%

Table S3: $\bar{\kappa}$ (time-averaged κ) calculated according to the well-mixed volume assumption with AMS-measured $\overline{m}_i$ as input listed in Table S2. κ_i is adopted from Table 1 of Petters & Kreidenweis (2007) for both the non-organic components and the organic one. The mass of NH_4^+ is divided to $(NH_4)_2SO_4$ and NH_4NO_3 by its molecular proportion assuming both sulfate and nitrate are fully neutralized as $(NH_4)_2SO_4$ and NH_4NO_3.

Case	Organic	$(NH_4)_2SO_4$	NH_4NO_3	$\bar{\kappa}$
ρ_i ($\mathrm{g\,cm}^{-3}$)	1.35	1.77	1.72	
κ_i	0.1	0.61	0.67	
0602	11.0%	82.3%	5.3%	0.55
0607	46.1%	46.5%	6.4%	0.35

Table S4: Aerosol perturbation induced percentage difference (PD) of LWP, CFC, RWP, N_c, r_{eff}, and SW averaged between 08:00 and 20:00 UTC for the 02 (Figure S16) and 07 (Figure S26) June 2021 cases. Note that time series of the cloudy-averaged N_c and r_{eff}, instead of the cloud-top averaged ones, are used for the PD calculation.

Case	$\mathrm{PD}_{\mathrm{LWP}}$	$\mathrm{PD}_{\mathrm{CFC}}$	$\mathrm{PD}_{\mathrm{RWP}}$	$\mathrm{PD}_{\mathrm{N_c}}$	$\mathrm{PD}_{\mathrm{r_{eff}}}$	$\mathrm{PD}_{\mathrm{SW}}$	$\Delta\mathrm{SW}$ [W m^{-2}]
02-06-2021	5.8%	-6.7%	-38.9%	52.7%	-6.6%	4.4%	-3.2
07-06-2021	-0.7%	1.6%	-17.4%	-31.6%	12.9%	2.7%	-0.8

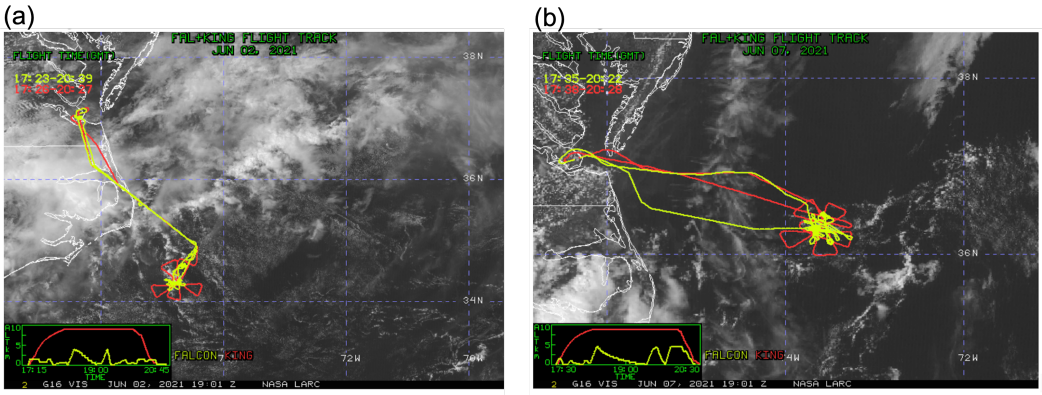

Figure S1: Visible images for (a): 02 and (b): 07 June 2021 cases from GOES-16 over the ACTIVATE measurement region. The embedded lower-left panels represent the flight altitude as a function of UTC time for the HU-25 Falcon (low-flying aircraft) and King Air (high-flying aircraft).

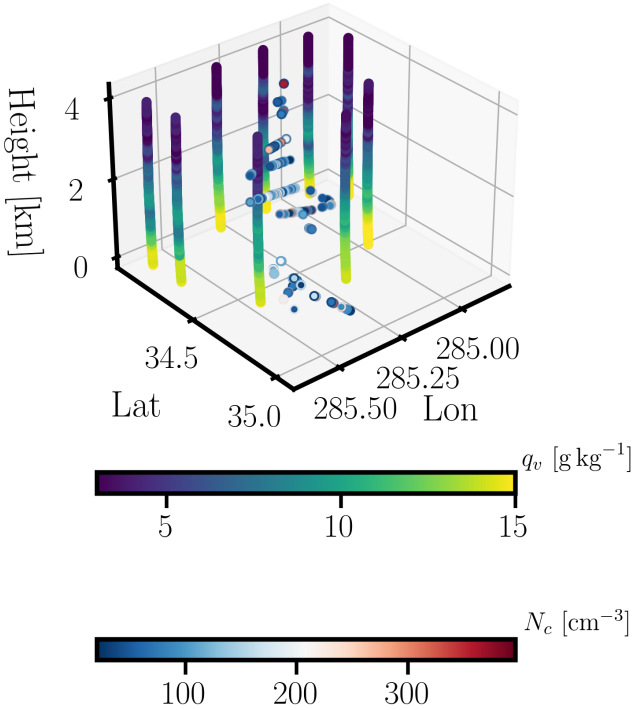

Figure S2: Water vapor mixing ratio (q_v) profile from dropsondes and N_c along the Falcon trajectory for the 02 June 2021 case from 18:29:20 to 19:46:16 UTC.

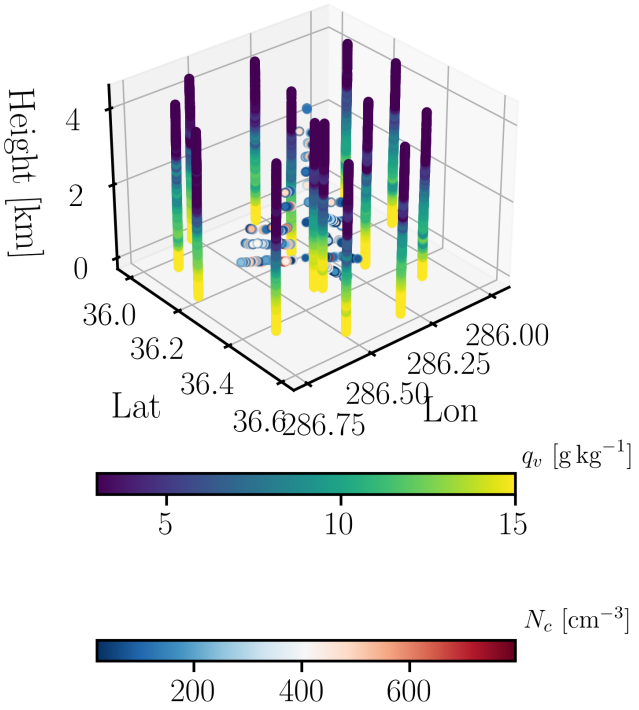

Figure S3: Same as Figure S2 but for the 07 June 2021 case from 18:25:54 to 19:45:37 UTC.

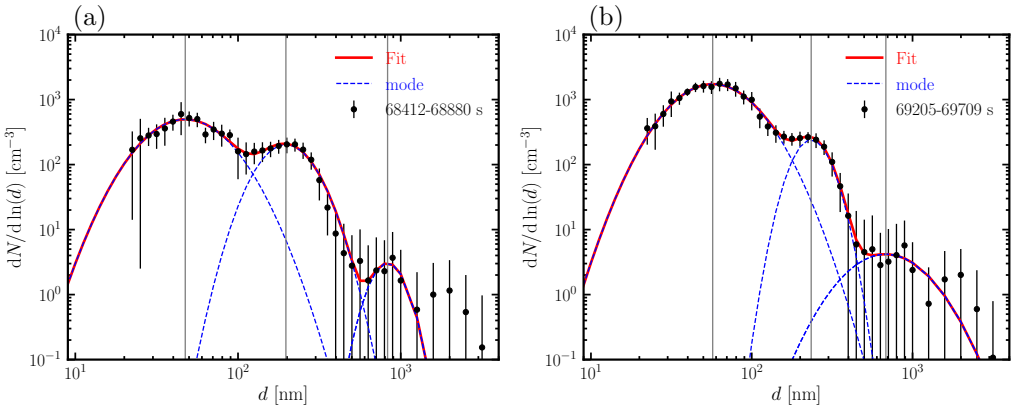

Figure S4: Aerosol size distributions (black dots) obtained from SMPS and LAS measurements for the 02 (a) and 07(b) June 2021 cases. The error bars indicate $\pm\sigma$ deviation from the time-averaged aerosol size distribution during a BCB flight leg. The red curve represents the final fitted size distribution. The dashed blue curves represent log-normal fitting of individual modes. Fitted parameters are listed in Table S1. Only particles with $d \geq 20$ nm are used for the fitting.

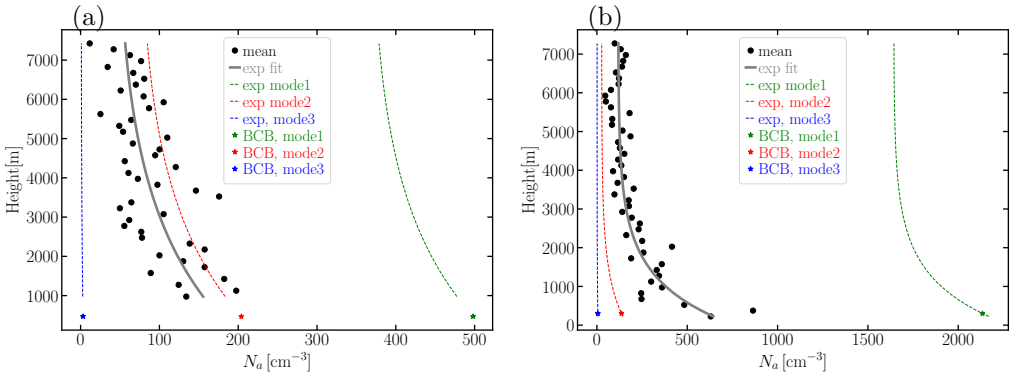

Figure S5: Time-averaged vertical profiles of N_a retrieved from the combined HSRL and RSP in the clear sky for the (a) 02 and (b) 07 June 2021 cases. These N_a retrievals are vertically-resolved from 75-8925 m with a horizontal spacing of 150 m. From in-situ measurements, three different aerosol size distribution modes are derived as described in Table S1. The retrieved vertical profiles of N_a that are closest to the BCB leg are selected for the time average: 68169–68324 s and 69209–69319 s since UTC 00:00 every 19 s for the 02 and 07 June 2021 case, respectively. The mean profile of RSP+HRSL N_a retrievals (black dots) are fitted using $N_a(h) = a\exp(-bh)+c$ (thick gray curve). The fitting parameters are $a = 154.827, b = 0.0003, c = 43.338$ and 642.910, 0.001, 117.940 for the 02 and 07 June cases, respectively. Following this exponential relationship, we obtain $N_a(h_{BCB})$ at the measured BCB height $h_{BCB} = 469$ m and 302 m for the 02 and 07 June cases, respectively. We apply this exponential decay fit to the aerosol modes derived from the in-situ measurements at h_{BCB} (stars). We thus shift mode 2 and 3 by $N_{2,3} - N_a(h_{BCB})$ (red and blue dashed lines) and scale mode 1 by a factor of $N_1/N_a(h_{BCB})$ (green dashed line) for the 02 June 2021 case. For the 07 June 2021 case, mode 1 and 2 are scaled by a factor of $N_{1,2}/N_a(h_{BCB})$ and mode 3 is shifted by a factor of $N_3 - N_a(h_{BCB})$. Modes 1 and 2 are scaled instead of shifted to avoid N_a decaying below zero. N_i $(i = 1, 2, 3)$ of the input aerosol size distributions follow the exponential decay (dashed lines) in the entire domain while the standard deviation σ and mean μ of the number concentrations are assumed to be constant based on the aerosol size distribution measured at the BCB leg. This exponentially decaying N_a is used in our LES because LES with uniformly distributed N_a in the entire domain tend to overestimate the observed N_c.

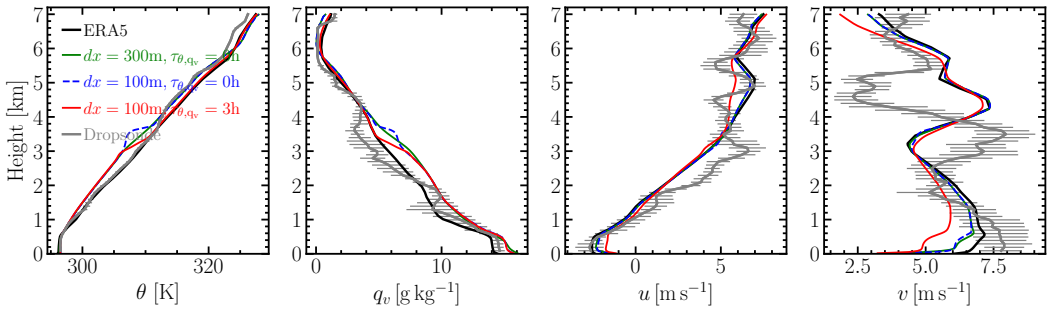

Figure S6: Domain-averaged vertical profiles from the WRF-LES simulation for different dx with the corresponding input forcings shown in Figure S23 at the measurement time for the 02 June 2021 case. The black line represents the ERA5 reanalysis data. The grey curves represent the dropsonde measurement with $\pm\sigma$ error bars. Except for a uniformly distributed aerosols in the domain, the same aerosol size distribution and $\bar{\kappa}$ as in the control simulations (Table 1) are used . For simulations represented by green and blue lines (lateral domain size 60 km), the $u\&v$ are nudged to ERA5 at a timescale of $\tau_{u\&v} = 1h$ over the entire domain. For the simulation represented by red lines (lateral domain size 20 km), $u\&v$ are nudged to ERA5 at a timescale of $\tau_{u\&v} = 3h$ above 3 km with a 100 m transition layer.

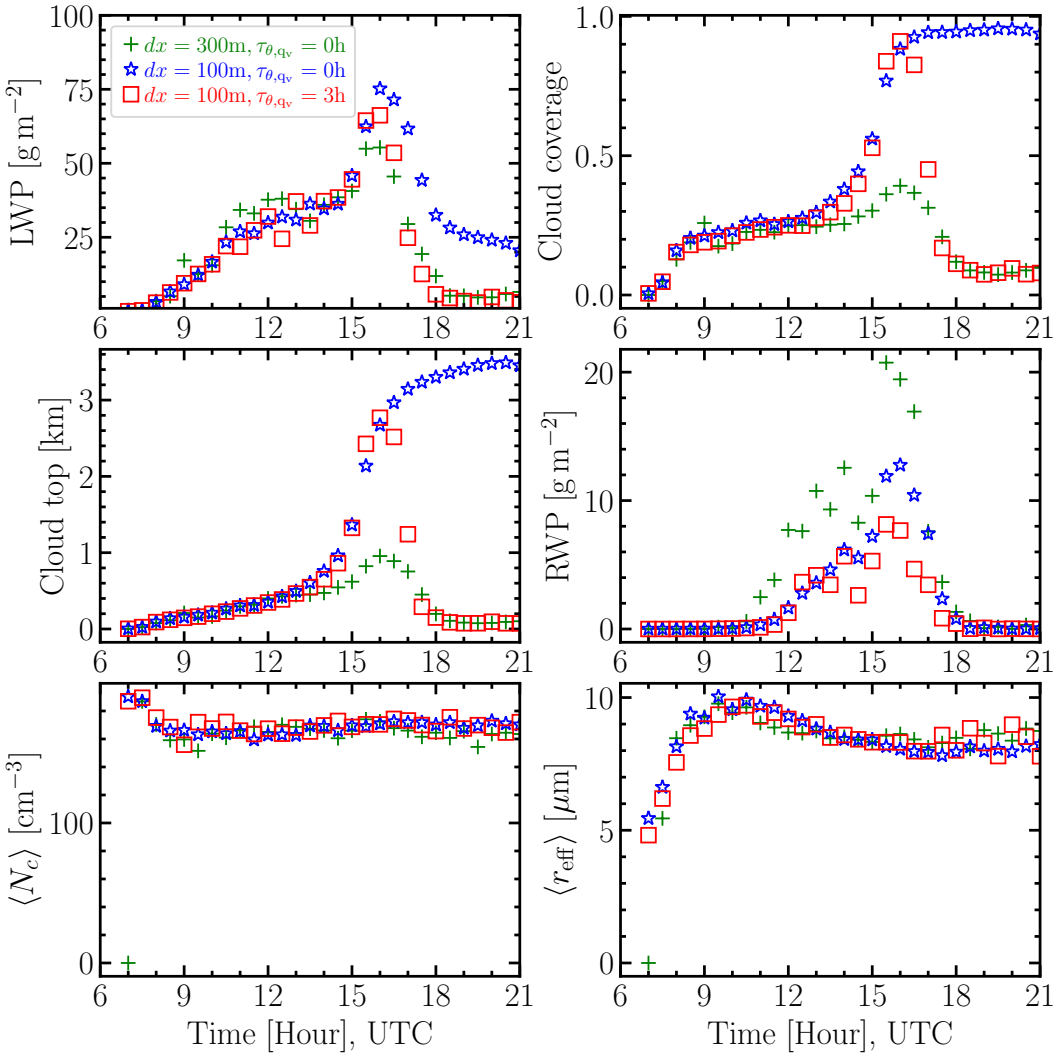

Figure S7: Corresponding time series of simulations shown in Figure S6. The LWP is domain averaged. The cloud top height is averaged.

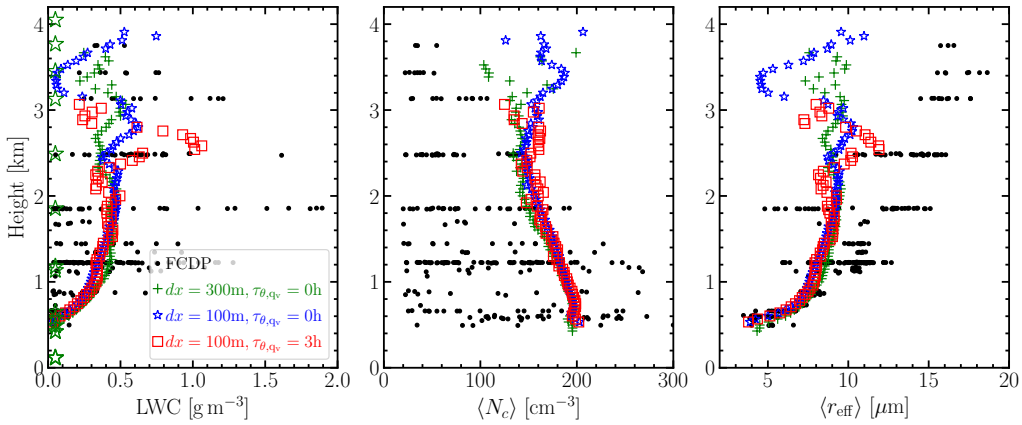

Figure S8: Comparison of vertical profiles of LWC, $\langle N_c \rangle$, and $\langle r_{\rm eff} \rangle$ amongst the simulations and the FCDP measurement. Same simulations as in Figure S6. Even though the simulation with $\tau_{\theta,q_v} = 0$ (blue stars) produces deeper clouds that are comparable to the FCDP measurement (black dots), it leads to a temperature inversion around 3.5 km (Figure S6) and unrealistic overcast conditions as in high clouds (Figure S7).

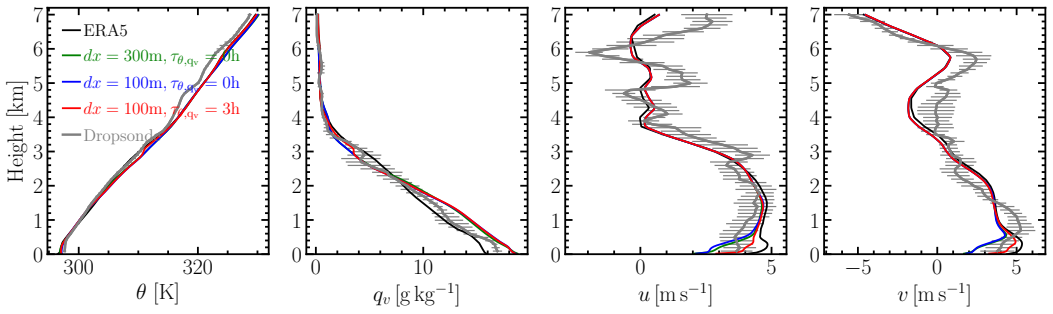

Figure S9: Domain-averaged vertical profiles from the WRF-LES simulation for different dx with the corresponding input forcings shown in Figure S23 at the measurement time for the 07 June 2021 case. The black line represents the ERA5 reanalysis data. The grey curves represent the dropsonde measurement with $\pm\sigma$ error bars. A constant N_c is used for all the simulations. For simulations represented by the green (lateral domain size 60 km) and blue lines (lateral domain size 20 km), the u&v are nudged to ERA5 at a timescale of $\tau_{u\&v} = 1$ h above 400 m with a 200 m transition depth. For the simulation represented by red lines (lateral domain size 20 km), u&v are nudged to ERA5 at a timescale of $\tau_{u\&v} = 3$ h above 3 km with a 100 m transition layer.

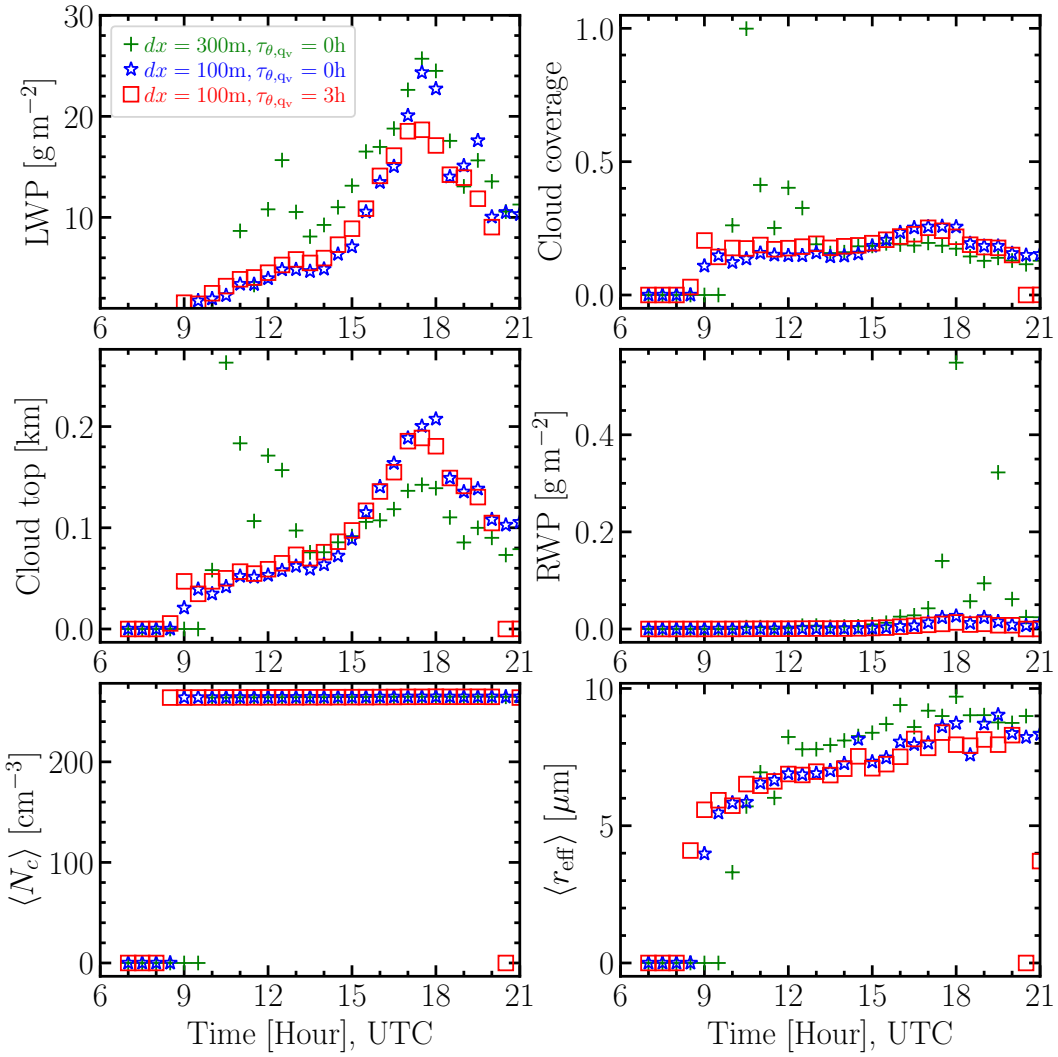

Figure S10: Corresponding time series of simulations shown in Figure S9. The LWP is domain averaged. The cloud top height is averaged.

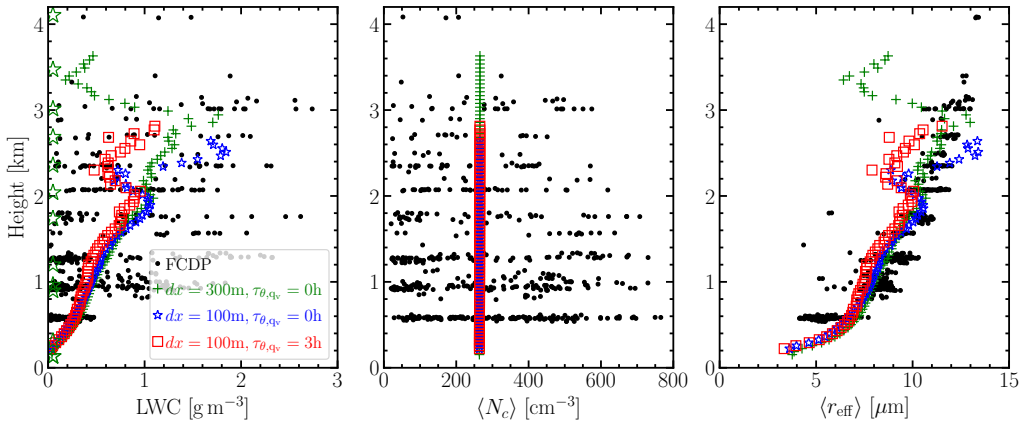

Figure S11: Comparison of vertical profiles of LWC, $\langle N_c \rangle$, and $\langle r_{\rm eff} \rangle$ amongst the simulations and the FCDP sampling. Same simulations as in Figure S9.

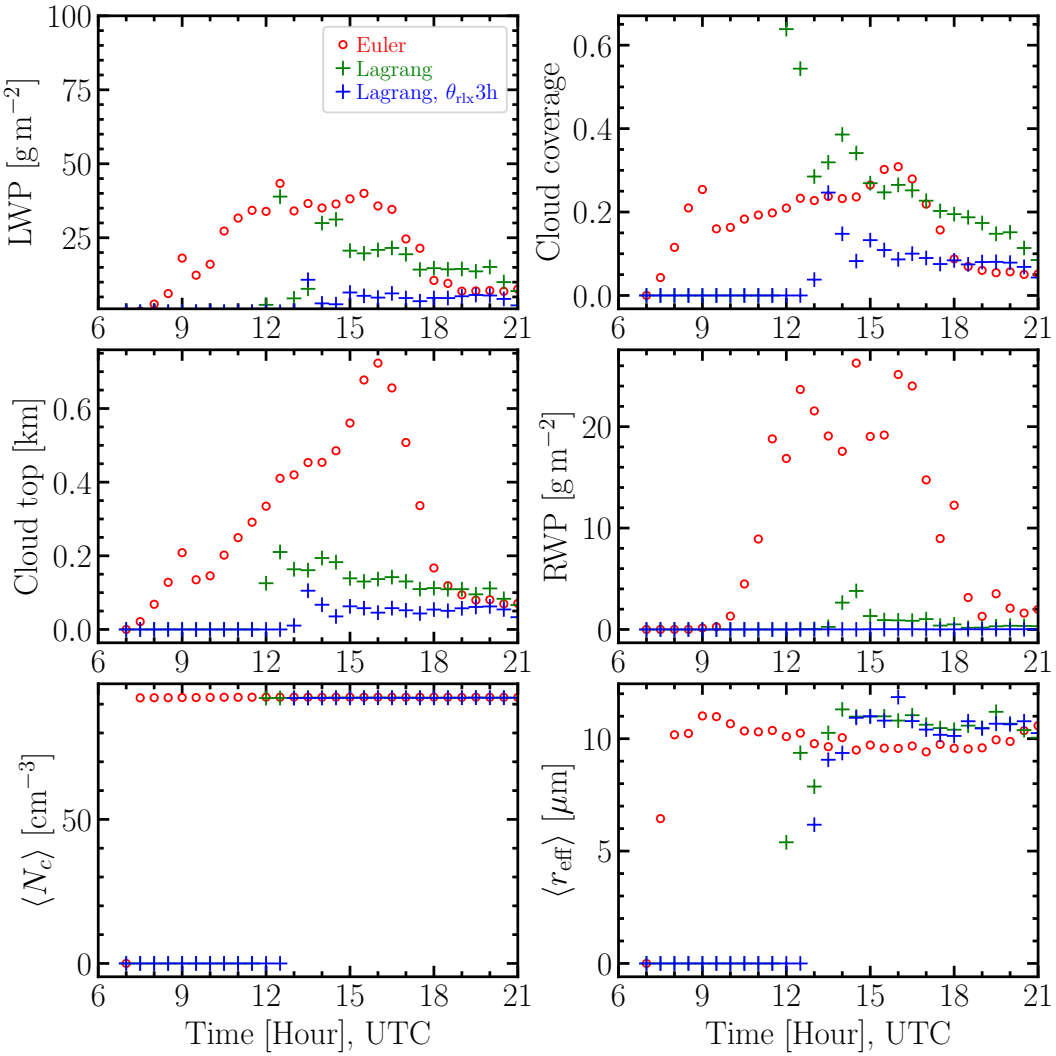

Figure S12: Comparison of time series between the Eulerian and Lagrangian forced LES for the 02 June 2021 case. A horizontal mesh grid spacing of $dx = dy = 300\,\mathrm{m}$ is adopted. Water path is domain averaged. The cloud top height is averaged. Cloud coverage is calculated by counting the vertical column where LWC $\geq$ LWC* $= 0.02\,,\mathrm{g\,kg^{-1}}$ (a column is defined as cloudy as long as one of its grids is cloudy), which is then normalized by the number of total vertical column of the entire domain. The Lagrangian trajectories starts from 34.44 N, 74.74W, and 1561.44 m altitude at 18:59:17 UTC. The blue curve is Lagrangian-forced with a 3-hour nudging to ERA5-θ. The input sounding of the Lagrangian simulation is the same as the Eulerian one (Dropsonde-area averaged ERA5 profiles at 6 UTC).

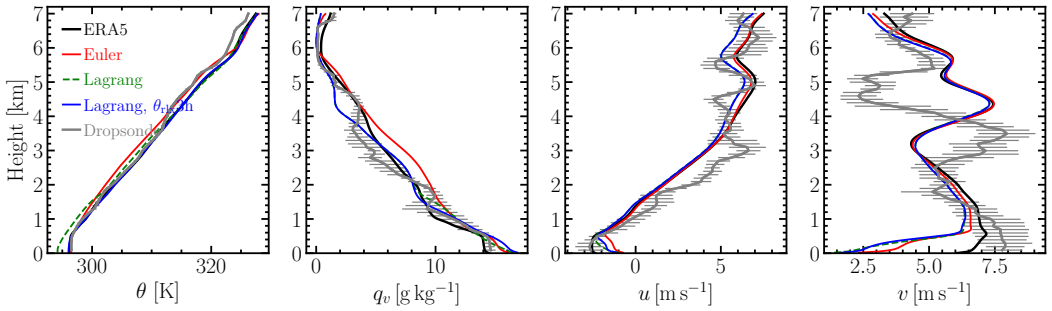

Figure S13: Evolution of domain-averaged vertical profiles from the WRF-LES simulation shown in Figure S12.

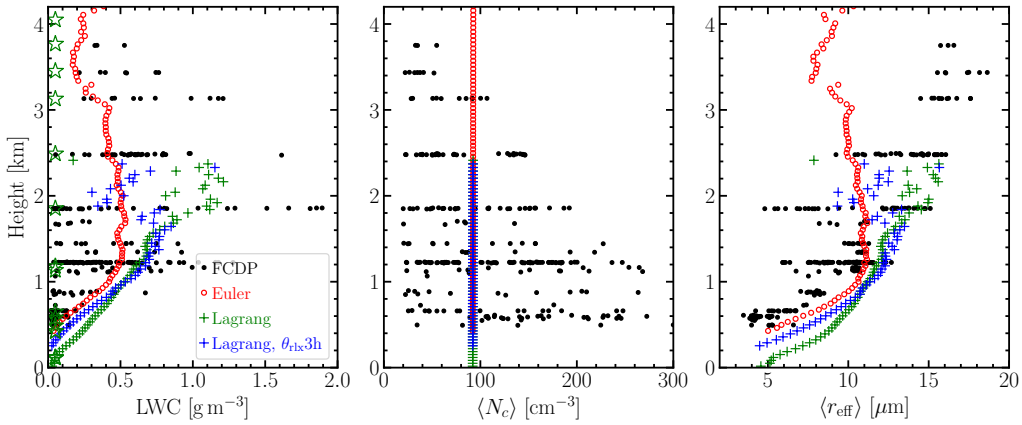

Figure S14: Comparison of vertical profiles of LWC, $\langle N_c \rangle$, and $\langle r_{\text{eff}} \rangle$ between the WRF-LES (same simulations as in Figure S12) and the FCDP sampling for the 02 June 2021 case. A threshold of LWC $= 0.02\,\text{g}\,\text{m}^{-3}$, $d_{\text{eff}} = 3.5\,\mu\text{m}$ and $N_c = 20\,\text{cm}$ is applied to both the WRF-LES and the FCDP sampling (black dots). The measurement took place between 18:29:20 to 19:46:16 UTC. The corresponding mean vertical profile of LWC, $\langle N_c \rangle$, and $\langle r_{\text{eff}} \rangle$ is obtained by averaging three snapshots of WRF-LES output as the output frequency is 30 minutes. The green stars mark all the flight legs above cloud base (ACB) and below cloud top (BCT).

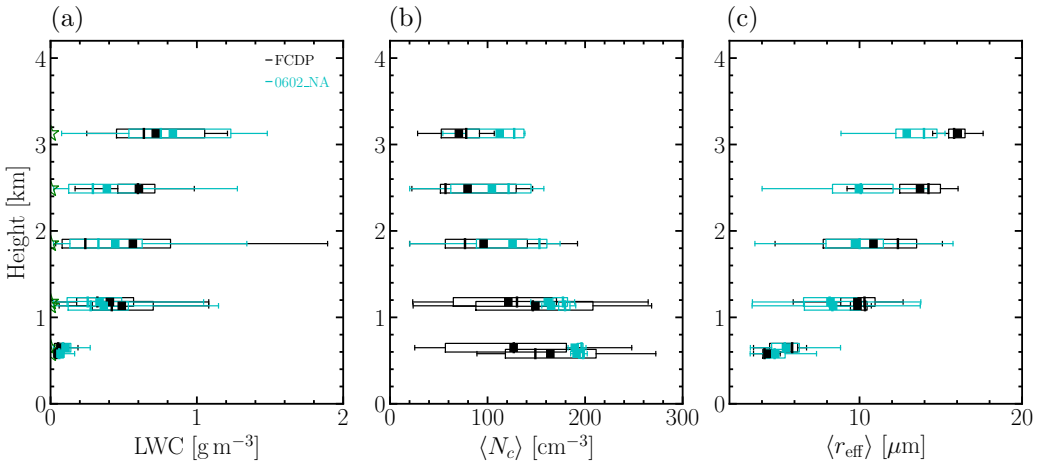

Figure S15: Corresponding statistics of Figure 3 for the 02 June 2021 case (simulation 0602_NA). Only flight legs (ACB and BCT) within clouds that have sufficient data (green stars) are used. The data are binned at those heights with a residual range of ± 50 m such that at least one model layer is counted at the height of each flight legs. Smaller residual ranges do not affect the statistics. In the box-and-whisker plot, the binned data extends horizontally from the 25th (Q1, l.h.s wall of the box) to the 75th (Q2, r.h.s wall of the box) percentile with the median represented by the splitting line inside the box, the mean represented by solid squares inside the box, the minimum ($Q_{\rm min}$) and maximum ($Q_{\rm max}$) values represented by the left and right end of whiskers, respectively, and the outliers (values larger than $Q_{\rm max}+1.5(Q2-Q1)$ and smaller than the $Q_{\rm min}-1.5(Q2-Q1)$) represented by open circles. Here Q denotes values of a quantity (i.e., LWC, $\langle N_c \rangle$, and $\langle r_{\rm eff} \rangle$).

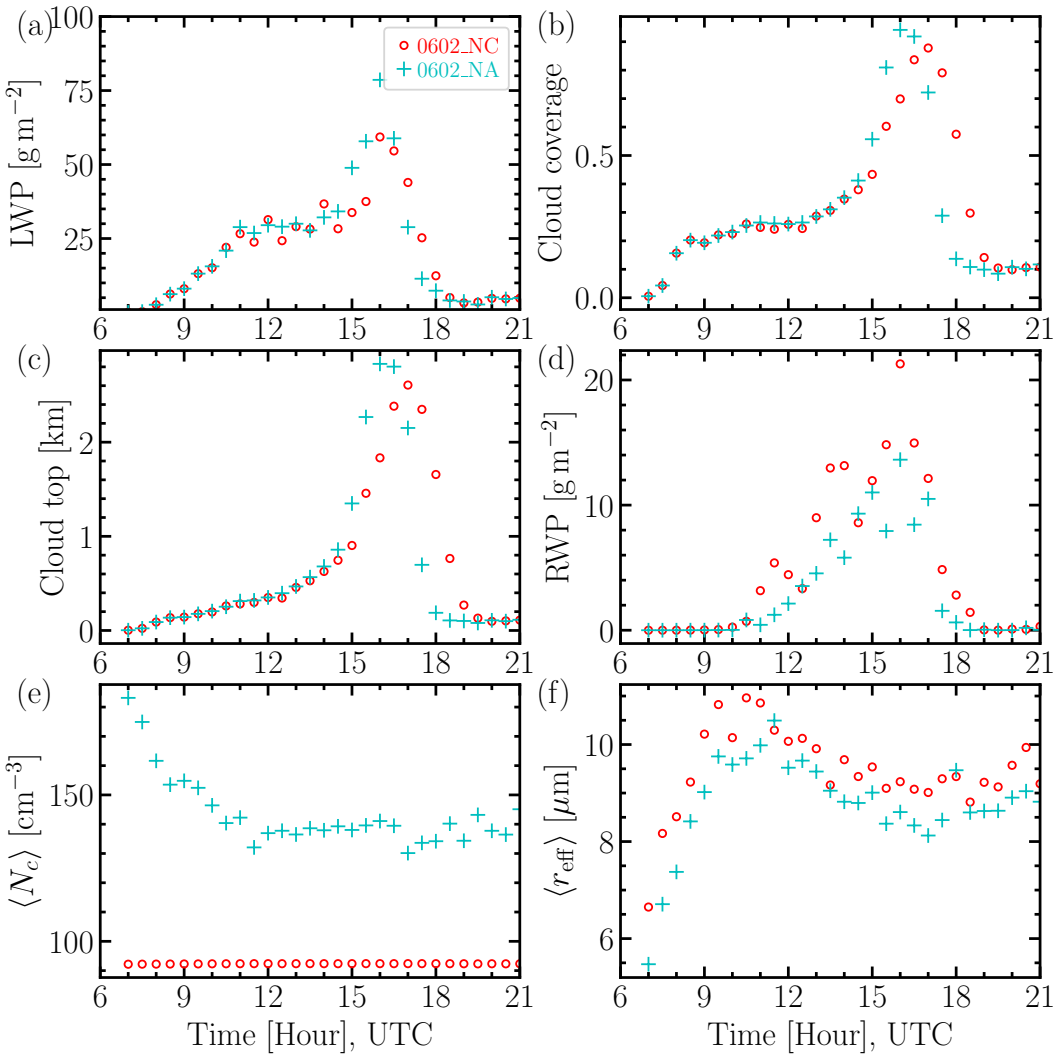

Figure S16: Time series for the 02 June 2021 case. Water path is domain averaged to compare to the ERA5. Cloud coverage is calculated by counting the vertical column where LWC $\geq$ LWC* = 0.02 g kg^{-1} (a column is defined as cloudy as long as one of its grids is cloudy), which is then normalized by the number of total vertical column of the entire domain. N_c and $r_{\rm eff}$ are cloudy-averaged. The cloud top height is averaged over the cloud system.

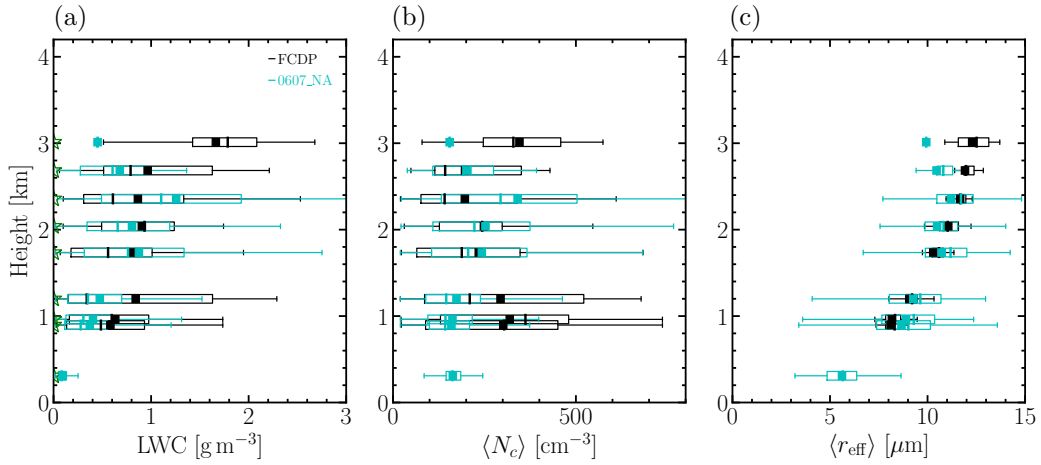

Figure S17: Corresponding statistics of Figure 7 for the 07 June 2021 case (simulation 0607_NA).

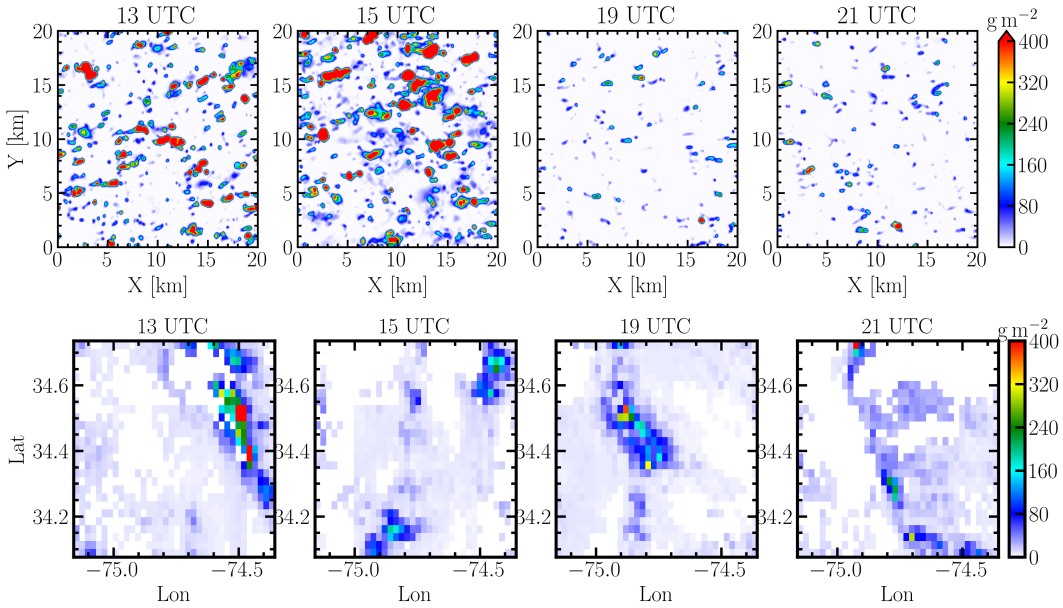

Figure S18: Spatial structure of LWP+RWP from simulation 0602_NA (upper row) and GOES-16 (lower row) for the 02 June 2021 case.

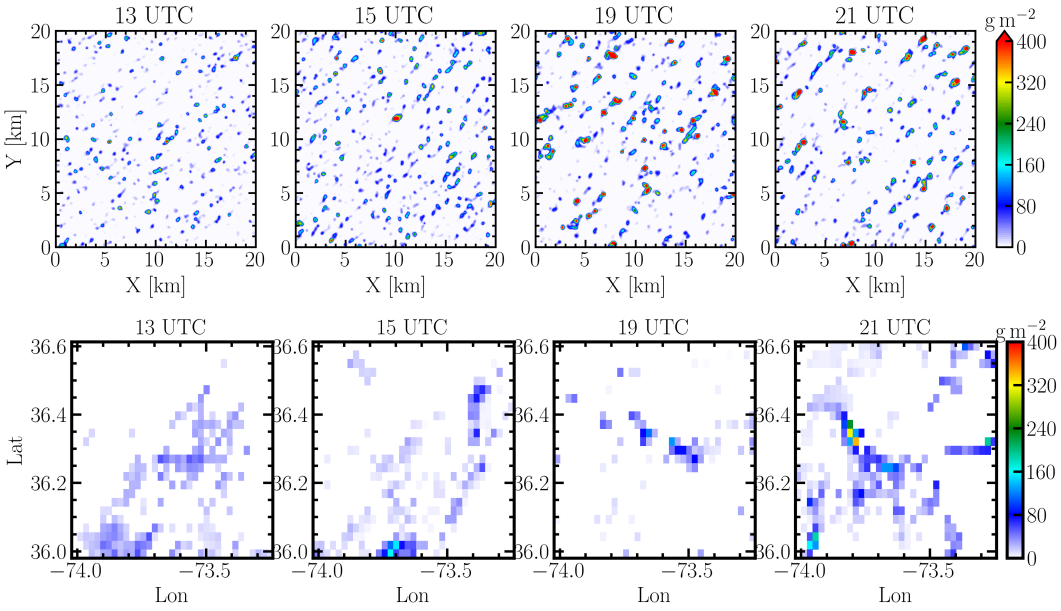

Figure S19: Same as Figure S18 but for the 07 June 2021 case.

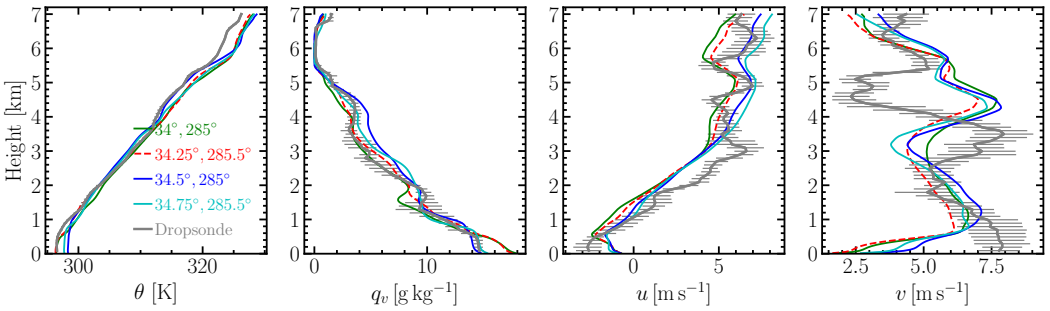

Figure S20: Domain-averaged vertical profiles from the WRF-LES simulation with the Eulerian input forcings at the location of individual dropsondes indicated in the legends from ERA5 for the 02 June 2021 case. The grey curves represent the dropsonde measurement with $\pm\sigma$ error bars. The lateral domain size is 60 km with $dx = dy = 300$ m. The u&v are nudged to ERA5 at a timescale of $\tau_{u\&v} = 1h$ above 400 m with a 200 m transition depth.

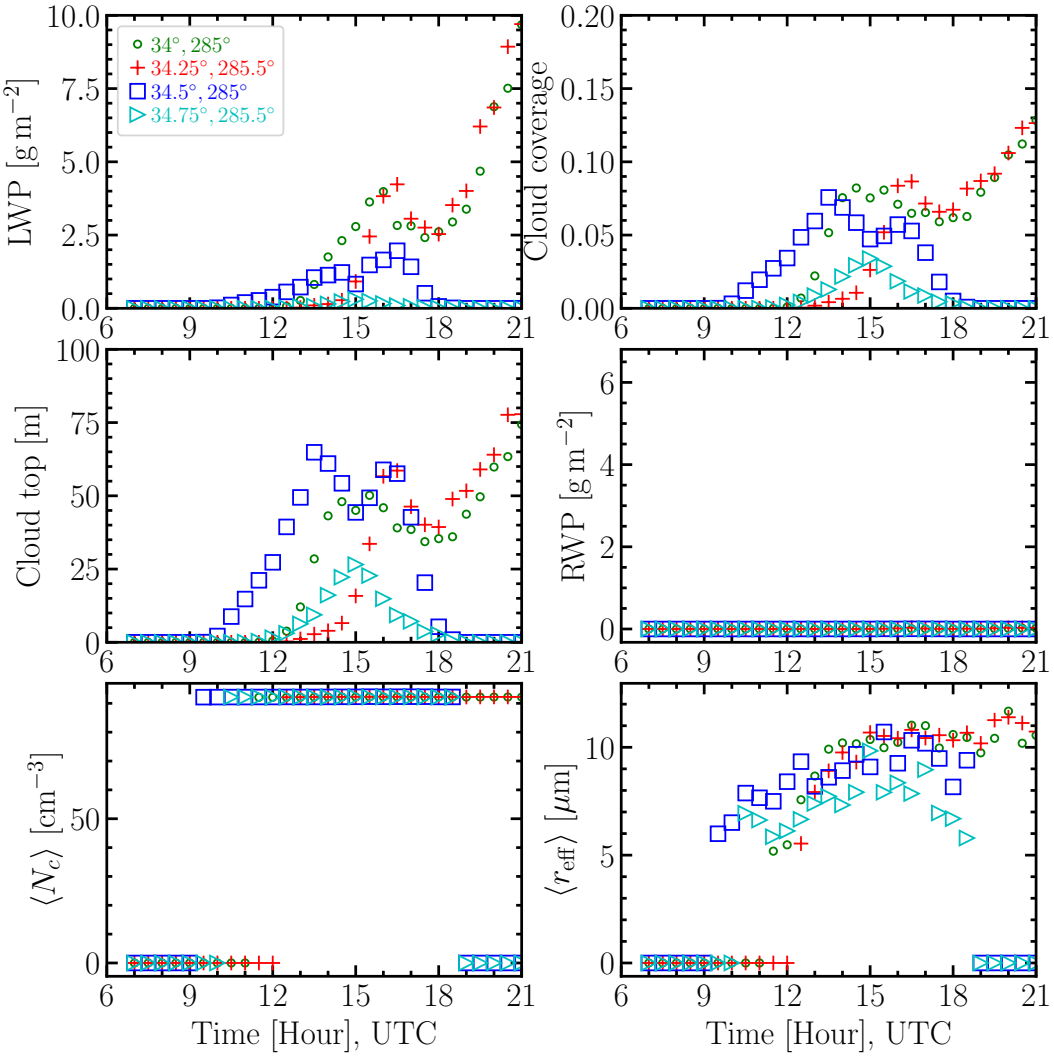

Figure S21: Corresponding time series of simulations shown in Figure S20. The LWP is domain averaged. The cloud top height is averaged.

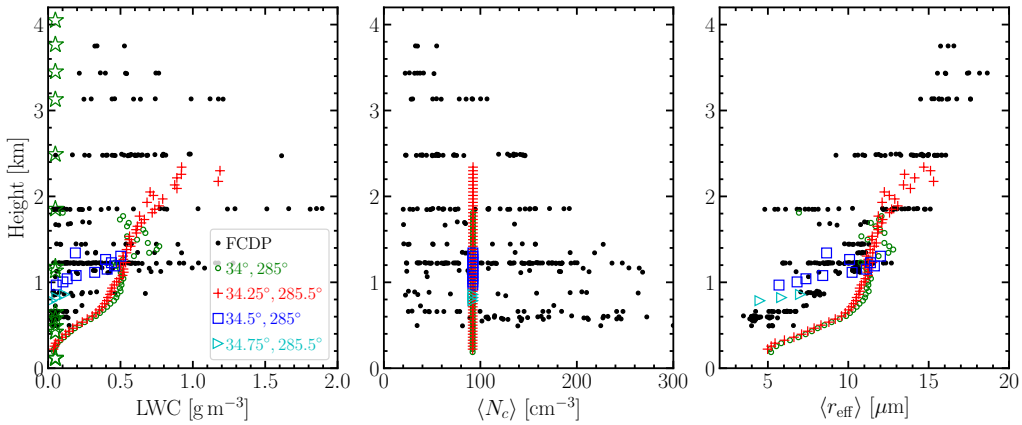

Figure S22: Comparison of vertical profiles of LWC, $\langle N_c \rangle$, and $\langle r_{\rm eff} \rangle$ amongst the simulations and the FCDP sampling. Same simulations as in Figure S20.

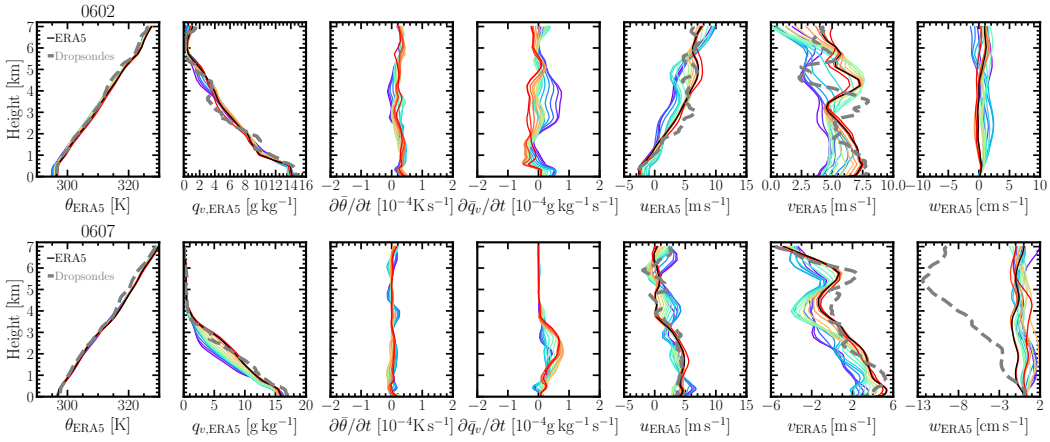

Figure S23: Hourly meteorological state and forcing profiles for the 02 (a) and 07 (b) June 2021 cases from ERA5 reanalysis data averaged precisely over the dropsonde-circle ($1° \times 1°$) area. The rainbow color scheme represents the time evolution (06:00-21:00 UTC): from purple to red. The averaged ERA5 reanalysis data over the measurement time period are marked by black lines, which are compared with the dropsonde measurements (dashed gray lines).

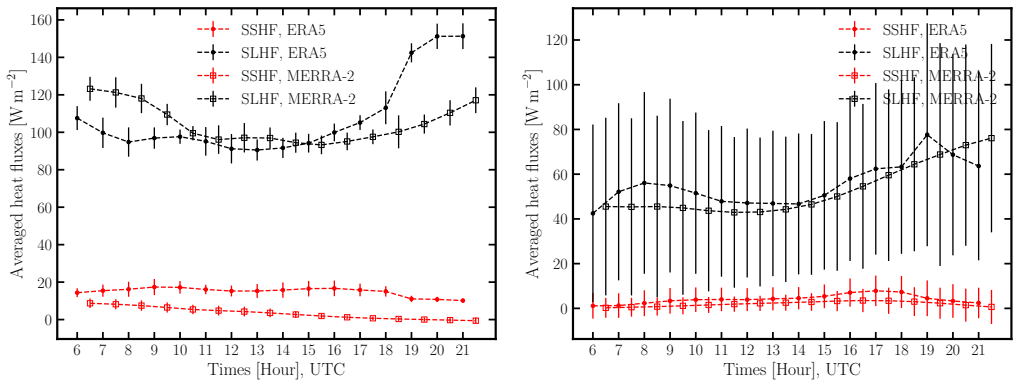

Figure S24: Averaged surface heat fluxes with $1-\sigma$ error bar from ERA5 reanalysis data over dropsonde-measurement area for the 02 (a) and 07 (b) June 2021 cases.

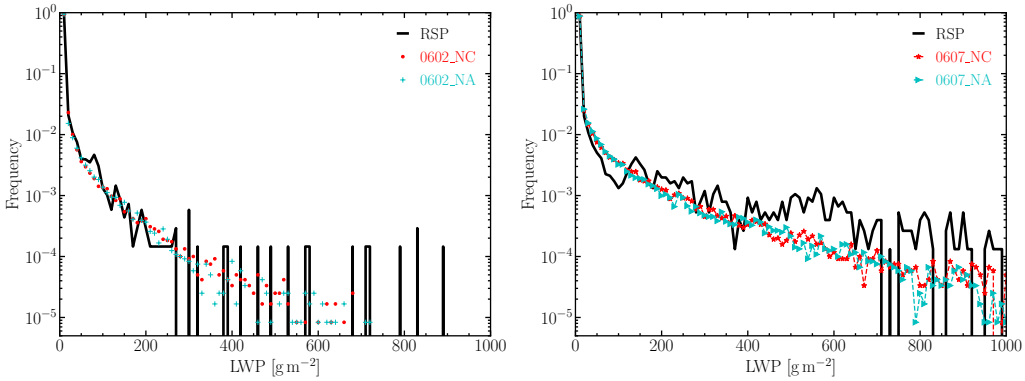

Figure S25: Validation of LWP frequency distribution from LES against the Research Scanning Polarimeter (RSP) measurements for the 02 (a) and 07 (b) June 2021 cases. The LES LWP frequency is averaged from three snapshots with a 30 minute time interval. The RSP sampling is averaged every 1 s such that it can be compared to LES with $dx = 100\,\mathrm{m}$; see details of the data processing of RSP measurments in (Li et al., 2023).

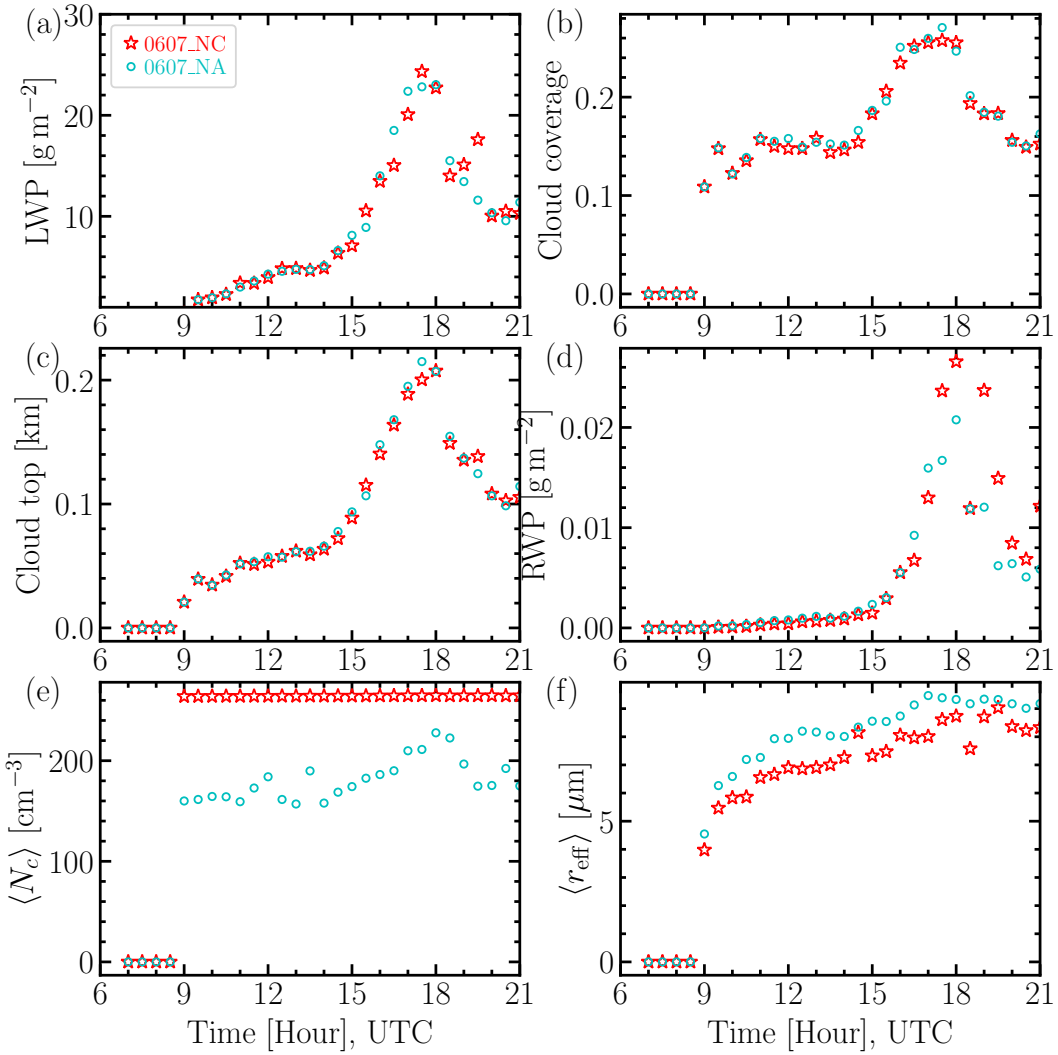

Figure S26: Same as Figure S16 but for the 07 June 2021 case.

References

Li, X.-Y., Wang, H., Chen, J., Endo, S., Kirschler, S., Voigt, C., ... Zeng, X. (2023, 1). Large-Eddy Simulations of Marine Boundary-Layer Clouds Associated with Cold-Air Outbreaks During the ACTIVATE Campaign. Part II: Aerosol–Meteorology–Cloud Interaction. *Journal of the Atmospheric Sciences*, *80*(4), 1025–1045. Retrieved from `https://journals.ametsoc.org/view/journals/atsc/aop/JAS-D-21-0324.1/JAS-D-21-0324.1.xml` doi: 10.1175/JAS-D-21-0324.1

Petters, M. D., & Kreidenweis, S. M. (2007, 4). A single parameter representation of hygroscopic growth and cloud condensation nucleus activity. *Atmospheric Chemistry and Physics*, *7*(8), 1961–1971. Retrieved from `https://acp.copernicus.org/articles/7/1961/2007/` doi: 10.5194/acp-7-1961-2007